Continuous increase in evaporative demand shortens the growing season of European ecosystems in the last decade

Mehdi Rahmati (mehdirmti@gmail.com)
Forschungszentrum Jülich GmbH https://orcid.org/0000-0001-5547-6442
Alexander Graf
Institute of Bio- and Geosciences: Agrosphere (IBG-3), Research Centre Jülich https://orcid.org/0000-0003-4870-7622
Christian Poppe Terán
Institute of Bio- and Geosciences: Agrosphere (IBG-3), Research Centre Jülich https://orcid.org/0000-0003-2283-0462
Wulf Amelung
Institute of Crop Science and Resource Conservation – Soil Science and Soil Ecology, University of Bonn
Wouter Dorigo
Vienna University of Technology https://orcid.org/0000-0001-8054-7572
Harrie-Jan Hendricks-Franssen
Forschungszentrum Jülich https://orcid.org/0000-0002-0004-8114
Carsten Montzka
Forschungszentrum Jülich GmbH
Dani Or
ETH Zurich https://orcid.org/0000-0002-3236-2933
Matthias Sprenger
Lawrence Berkeley National Laboratory,
Jan Vanderborght
Forschungszentrum Jülich GmbH
Niko Verhoest
Ghent University https://orcid.org/0000-0003-4116-8881
Harry Vereecken
Institute of Bio- and Geosciences: Agrosphere (IBG-3), Research Centre Jülich https://orcid.org/0000-0002-8051-8517

Article

Keywords:

Posted Date: October 19th, 2022

DOI: https://doi.org/10.21203/rs.3.rs-2162650/v1

Version of Record: A version of this preprint was published at Communications Earth & Environment on July 3rd, 2023. See the published version at https://doi.org/10.1038/s43247-023-00890-7.

Abstract

Although it has been shown that climate warming has steadily increased the length of the growing season (LGS) in Europe, we present new evidence that this trend reversed during last decade. Warmer European winter and spring weather combined with adequate soil moisture still results in early greening, albeit at slower rates than in the past. However, the recent (2014-2020) accelerated shift toward earlier onset of dormancy has resulted in a shortening of LGS compared to previous years. The results show that this is mainly due to higher atmospheric water demand (AWD) in summer. The higher AWD stresses the vegetation even though there is still enough water, but the vegetation cannot provide the needed water for transpiration because the water transport system is inadequate, or the root system is adapted to conditions other than the current condition. Our results have implications for future management of European ecosystems in a warmer world.

introduction

Vegetation phenology is a sensitive indicator of changes in climatic conditions[1-5]. The timing of leaf unfolding in deciduous vegetation, so-called onset of greening (OG), in spring[6-8] and onset of dormancy (OD) in autumn are among the most important phenological events marking the growing season (GS) in mid- and high- latitudes[9-11]. Global warming, particularly in the Northern Hemisphere, is leading to an earlier onset of the vegetation cycle, as evidenced by both ground measurements[9,12-14] and satellite-based monitoring of land surface greenness[15,16]. Although the results for early OG are in good agreement, conflicting assessments have been made when evaluating the impact of global warming on the timing of OD, with some reporting delayed OD[7,17,18] and others reporting earlier OD[19,20]. Delayed OD is most likely due to increased photosynthetic enzyme activity[21], decreased chlorophyll degradation rate[22], decreased likelihood of exposure to frost in the autumn[23,24], or increased capacity for growth and photosynthetic consumption, all caused by increased temperature (T) [17]. In most cases, earlier OD is due to limited leaf life[19] or lower plant productivity later in the season due to water deficits[20]. A potential explanation for climate change and soil moisture (SM) changes during GS and their effects on OG and OD is provided in Fig. 1.

Some observations in the northern hemisphere[25] show that during the period 1982-2011, earlier OG and increased evapotranspiration (ET) in spring resulted in an additional deficit in SM in summer, which might result in an earlier OD. However, the impact of a summer SM deficit on OD due to an ET increase needs to be supported by an analysis of the long-term relationships between ET, SM and OD. Though, it is not only ET that determines SM and OD, but also precipitation (P) since lower P at unchanged ET results as well in lower SM and possibly earlier dormancy. Another possible scenario is that neither P nor SM show a significant change but increased atmospheric water demand (AWD), e.g., increased vapor pressure deficit (VPD) as a measure of AWD, could disrupt the soil-plant-atmosphere water chain and then regulate stomatal closure and OD. This could, but need not, be accompanied by increased ET, since a simultaneous increase in AWD and partial closure of the stomata may result in no change in ET.

Therefore, it is important to investigate whether reduced SM leads to earlier OD or whether increased AWD are intolerable for certain vegetation types even though SM remains constant. To do this, one may consider the seasonal variations of VPD and SM as well as their interactions with OG and some meteorological variables such as P, T, and ET.

In general, there are several mechanisms that cause dormancy, including 1) low T, 2) water deficiency (caused by increased ET or decreased P, or a combination of both), 3) maximum leaf age (earlier OG leads to earlier OD), and 4) other plant stressors (heat stress or breakdown of xylem capillaries due to high AWD). Climate change can affect all four of these causes, and some may act in opposite directions. For example, higher T in fall may delay OD, while an increase in P deficit may result in earlier OD. Therefore, the objectives of our analysis were to investigate 1) whether our data confirm previous findings on the shift in OG, OD, and consequently LGS in Europe for the period 1982 to 2020, 2) whether meteorological variables along with SM data provide explanations for possible shifts, and finally 3) whether the water or energy supply is the main controlling factor in LGS changes.

Results

Figure 2 illustrates the spatial variation of the long-term (1982–2020) LGS mean for Europe as a simple derivative of OD and OG data (see supplementary Fig. 1). To obtain these results, we applied the innovative LFD NDVI method (see details in Methods) to long-term (1982–2015) GIMMS[26,27] NDVI data augmented by AVHRR[28] (1982–2017) and MODIS[29] (2001–2020) NDVI data. Then, using the Mann-Kendall test[30,31] (see Methods), we examined a possible trend in the LGS, OG, and OD data from 1982 to 2020. Our analysis confirms previous reports of early greening in Europe[11,32] showing a significant trend towards earlier greening in 35% of pixels (see supplementary Fig. 2a), with OG shifting from mid-April in the first period (1982–1990) to early April in the last period (2011–2020), resulting in an average of 11 days earlier greening in these pixels. For 63% of the pixels, there is no significant trend, but still a backward shift of up to 3 days. Only 2% of pixels show a significant trend toward later OG, with OG shifting on average by 16 days from early April in 1982–1990 to mid-April in 2011–2020. The amplitude of the shift (3 to 11 days per total period, equivalent to ~ 1 to 3 days per decade) is within the range of values reported by other researchers[8,25,33] reporting an earlier OG from ~ 1 to ~ 5 days per decade.

The results indicate that OD shows a more complicated response to climate warming than OG. 73% of the pixels show no significant trend in OD data (see supplementary Fig. 2b), with OD almost fixed to October 13 (± 1 day). 17% of the pixels show earlier OD, shifting from mid-October in 1982–1990 to early October in 2011–2020, while the opposite trend (shifting to later days) is observed in 10% of pixels. In contrast to ours, Liu et al. [17] using the same GIMMS NDVI data, observed a trend toward later OD at ~ 70% of Northern Hemisphere pixels between 1982 and 2011 (at a mean rate of 0.18 ± 0.38 d/y). Other studies, e.g., Julien and Sobrino [33], also using the same GIMMS NDVI data and examining the period 1981–2003, show a later OD, but on a global scale.

Finally, almost two-third of the pixels (65%) showed no significant trend in LGS (Fig. 3), as the LGS is almost fixed at 185 days (± 1 day). 28% show a lengthening trend where the LGS has increased on average by almost 13 days from 177 to 190 days, and 7% show a shortening trend where the LGS has decreased by a mean of 16 days from 194 to 178 days. Julien and Sobrino [33] used the same GIMMS NDVI data as we used, but a shorter period from 1981 to 2003. In their analysis LGS increased by 0.8 d/y worldwide. Similarly, Stöckli and Vidale [34] found an increase of 0.96 d/y for Europe during 1982–2001 period. Other researchers[15,35,36] also report increasing LGS in the Northern Hemisphere in earlier decades (before 2010). For our longer period (1982–2020) and Europe, the average increase is only one third of the reported values (~ 0.3 d/y), and a lengthening occurs in only 28% of the pixels. In agreement with our results, Garonna et al. [37] showed that the LGS increased significantly from 1982 and 2011 only over 18–30% of the European land area. It seems that including more recent years in analysis diminishes the lengthening trend in LGS and the percentage of the land surface over which it occurs, indicating that the trend has changed more recently. Based on supplementary Fig. 3a showing the spatial patterns of the long-term (1982–2020) trend slope of LGS data, central Europe mainly shows lengthening trends for LGS with trend slopes varying between 0 to 1 d/y while the lower latitudes along with higher latitudes show a shortening trend in LGS data (see supplementary Fig. 3b, c to find out about the spatial patterns of OG and OD).

As part of a periodic trend analysis, we examined the hypothesis of whether the trend slope of the LGS (as well as the OG and OD) varied across the 1982–1990, 1991–2000, 2001–2010, and 2011–2020 time periods. Interestingly, Europe shows a positive mean LGS trend slope of 0.43 and 0.35 d/y in the first and second periods, respectively, which can lead to about one week longer seasons at the end of the second period (Fig. 5). The trend falls to zero in the third decade (2001–2010), but with a tendency toward negative values. In the last decade, however, the trend changes to negative, with a mean trend slope of -0.12 d/y, which offsets almost one-third of the shift in the first decade. Almost the same behavior (positive trends of LGS in the first two periods and negative trend in the last decades) is seen in croplands, evergreen needle leaf forests, and grasslands. However, it appears that wooden tundra, mixed forests, and open shrublands shows a continues lengthening trend for LGS except for a negative trend in second decade in open shrubland. The mixed tundra is also an exception, where we see a positive trend in the last period (2011–2020) and negative trends in the remaining periods. Excluding open shrublands and tundras, the strongest negative trend in the last period is observed in grasslands with a rate of -0.50 d/y, followed by croplands and evergreen needleleaf forests with a rate of -0.29 ± 0.01 d/y. A pessimistic projection of these results could therefore lead to the conclusion that we face a further decrease in LGS in most of vegetation types in Europe after 2020, due to the severe dry and warm years that occurred since then.

While Europe has experienced an average trend of -0.31 d/y for the OD over the last period (2011–2020), in this period there has been almost less shift in the OG with a trend slope of -0.19 d/y (see supplementary Figs. 4 and 5). This reverses the trend of LGS over the last period and offsets the lengthening of LGS in previous periods. However, to determine when such a trend reversal in LGS (and OG

and OD) occurs, we performed another trend analysis, this time setting the data period to a 15-year window and shifting the window across different years from 1982–2020 and conducting trend analysis over these data. In this way we can see which year is critical and at what time the reversal occurs. The results (Fig. 5) show that the reversal in LGS trend occurs after 2003–2004, probably due to the severe drought we had in Europe in 2003. However, we still see a positive trend for LGS till 2013–2014, meaning that the growing season is still lengthening, albeit at a slower rate. However, after 2014 the trend becomes negative, which means that from then on the length of the season is shortened.

In this suction, we determined control factors (see supplementary Figs. 6 to 8) for anomalies (Δ) in the OG and OD as well as LGS using the GMDH[38] framework (see Methods) together with the main meteorological variables (T, P, and VPD) and surface SM (SSM) and root zone SM (RSM) from GLDAS-NOAH[39–41], ERA5-Land[42], and GLEAM[43,44]. All variables are averaged for winter [January 1 until 30 days before OG], early spring [30 days before the OG to OG], spring [OG to the peak of greening, PG], summer [PG to until two weeks before the OD], and late summer [two weeks before the OD to OD] times.

Our analyses shows that ΔT and ΔVPD in late summer beside ΔT in early spring and spring are the most important control factors for LGS (supplementary Fig. 6). For almost 28% of the pixels, late summer ΔT is the first important factor entering the model. For nearly 13% of the remaining pixels, it is also important as a second control factor. Similarly, ΔT in early spring is the first and second important factor entering the model for nearly 12 and 8% of the pixels, respectively. Overall, for almost 54% of the pixels, ΔT (either in spring or summer) is the most important factor for LGS. For 40% of the remaining pixels, ΔT is still the second most important factor for LGS.

ΔVPD in late summer is the second important variable for the model. For almost 16% of pixels, ΔVPD in late summer is the most important control factor of the LGS, while for 10% of pixels it is the second most important control factor. Regardless of the period for which an average is taken, ΔVPD is the first and second important control factors for LGS for nearly 29 and 22% of pixels, respectively. Finally, ΔP is the third most important variable controlling LGS, being the first control factor for almost 10% of pixels and the second for 15%. ΔSM (both at the surface and in the root zone) clearly have the least influence on LGS.

Looking at the control factors for OG and OD, we find that ΔT and ΔVPD in early spring are the most important control factors for OG (see supplementary Fig. 7a) and ΔT in late summer and summer along with ΔVPD in late summer are the most important control factors for OD (see supplementary Fig. 7b). This means that the availability of SM to plants is the least limiting factor for plant growth in Europe, even though climate change has probably altered P patterns in Europe. This shows that, in contrast to other publications[20] citing SM deficit (especially in summer) as the most important factor driving changes in OD, at least SM availability has not played such a prominent role in Europe until 2020. This conclusion raises the question: If SM is less of a constraint, why did we still observe a shortening of LGS during recent years, even though OG still shifted to earlier dates, albeit at a slower rate? A possible answer is that AWD was increased due to warmer conditions (reflected in increased average T and VPD), and

water supply was therefore below plant water demand (caused by higher AWD), which led to earlier OD. A principal component analysis (PCA) between OG and other variables (supplementary Fig. 9a) showed that OG is negatively correlated with T, VPD and P in winter and early spring, while other variables, including SSM and RSM, are not correlated with OG. This means that the higher T, VPD, and P are in winter and early spring, the earlier OG is reached. In a similar analysis (supplementary Fig. 9b), OD shows a negative correlation with VPD and T in summer and late summer and a positive correlation with P in all periods, i.e., the higher VPD and T are in summer and late summer, the earlier OD is reached or the higher the P, the later the OD is reached. As mentioned earlier, there is no significant correlation between OD and other variables, especially SSM and RSM.

There may be different reasons for the observed behavior for different land use types. In general, Europe-wide trends in OG are driven to a large extent by the pattern observed for forested and mixed tundra (supplementary Fig. 4). These high-latitude ecosystems are very sensitive to climate change, so a few degrees of warming have a greater impact there than in temperate regions[46]. This likely explains that why early spring T is the most important controlling factor for the OG (supplementary Fig. 7a) and, consequently, one of the two most important variables in explaining LGS. Similarly, the earlier OD is primarily due to cropland and grassland, which are generally expected to have shallower root systems than the other woody land-use classes. It is therefore not surprising that late summer T and VPD were the most important and second most important variables for these land uses, as grasses and cropland will suffer drought first. To address this, we examined the control factors of LGS (as well as OG and OD) in different land use types (results not shown). In the case of LGS, these are almost the same factors as Europe that play a role within the different vegetation types, except for tundra (both wooden and mixed) and to some extent for evergreen needle leaf forests. For evergreen needle leaf forests, the only difference is that late summer ΔVPD plays a lesser role and dominates in 14% of the pixels of this land cover, compared to 26% in Europe. For mixed and wooden tundras, the importance of late summer variables for LGS decreases even more. The other dominant land cover types in Europe, including cropland, mixed forest, grassland, and open shrubland, show almost the same behavior as we observed for Europe as a whole. Almost the same results were also obtained for OD and OG (not shown).

To support the results of the GMDH analysis, we performed an additional trend analysis over late summer ET, RSM, SSM, T, VPD, and P data. Results show no trend for SSM, RSM, P, and ET, but increasing trends for T and VPD in majority of pixels in Europe, which is consistent with our previous reports. This is confirmed by both reanalysis (see supplementary Table 1) and in situ data (supplementary Fig. 10). A supplementary discussion is also provided in supplementary information.

The ecohydrological feedback we highlighted in our research (onset of wilting/senescence at higher SM when ET is higher) is already well documented. For example, in one of the first studies on the relationship between ET and SM, Brown [47] experimentally showed already 110 years ago that the transpiration rate affects the SM threshold at which wilting occurs. If the transpiration rate is high, plants will wilt at a higher SM, while at a lower transpiration, plants will gradually be able to absorb more water from the soil, so that wilting will occur only when the SM is lower. Gao et al. [48] also noted that OD occurs earlier despite

having still sufficient SM, but the plant's root systems are adapted to extracting the amount of water that is normally required and that amount changes probably due to increased VPD.

Our results implicate that changes in OG and OD and consequently in LGS will directly affect the net carbon balance of the ecosystem[49–51], the exchange of water and energy with the atmosphere[52] and management of ecosystems but the impact of these changes is not yet accounted for in land surface models. To cope with these changes agricultural management practices will need to be adapted in terms of suitable crop selection and breeding (e.g., optimally designed root systems), crop rotation and intercropping (e.g., avoiding bare soil) and irrigation management to optimally exploit the change in LGS.

References

1 Zhu, K. Preliminary study on the climate change in China during last 5000 years. *Science in China (in Chinese)* **2**, 168-189 (1973).

2 Lieth, H. in *Phenology and seasonality modeling* 3-19 (Springer, 1974).

3 Schwartz, M. D. Green-wave phenology. *Nature* **394**, 839-840 (1998).

4 Menzel, A. & Fabian, P. Growing season extended in Europe. *Nature* **397**, 659-659 (1999).

5 Beaubien, E. & Freeland, H. Spring phenology trends in Alberta, Canada: links to ocean temperature. *International Journal of Biometeorology* **44**, 53-59 (2000).

6 Cleland, E. E., Chuine, I., Menzel, A., Mooney, H. A. & Schwartz, M. D. Shifting plant phenology in response to global change. *Trends in ecology & evolution* **22**, 357-365 (2007).

7 Richardson, A. D. *et al.* Climate change, phenology, and phenological control of vegetation feedbacks to the climate system. *Agricultural and Forest Meteorology* **169**, 156-173 (2013).

8 Piao, S. *et al.* Plant phenology and global climate change: Current progresses and challenges. *Global change biology* **25**, 1922-1940 (2019).

9 Menzel, A. *et al.* European phenological response to climate change matches the warming pattern. *Global change biology* **12**, 1969-1976 (2006).

10 Peaucelle, M. *et al.* Spatial variance of spring phenology in temperate deciduous forests is constrained by background climatic conditions. *Nature communications* **10**, 1-10 (2019).

11 Kern, A., Marjanović, H. & Barcza, Z. Spring vegetation green-up dynamics in Central Europe based on 20-year long MODIS NDVI data. *Agricultural and Forest Meteorology* **287**, 107969 (2020).

12 Schwartz, M. D., Ahas, R. & Aasa, A. Onset of spring starting earlier across the Northern Hemisphere. *Global change biology* **12**, 343-351 (2006).

13 Fu, Y. H. *et al.* Recent spring phenology shifts in western C entral E urope based on multiscale observations. *Global ecology and biogeography* **23**, 1255-1263 (2014).

14 Peñuelas, J. & Filella, I. Responses to a warming world. *Science* **294**, 793-795 (2001).

15 Barichivich, J. *et al.* Large-scale variations in the vegetation growing season and annual cycle of atmospheric CO2 at high northern latitudes from 1950 to 2011. *Global change biology* **19**, 3167-3183 (2013).

16 Piao, S. *et al.* Leaf onset in the northern hemisphere triggered by daytime temperature. *Nature communications* **6**, 1-8 (2015).

17 Liu, Q. *et al.* Delayed autumn phenology in the Northern Hemisphere is related to change in both climate and spring phenology. *Global change biology* **22**, 3702-3711 (2016).

18 Forkel, M. *et al.* Codominant water control on global interannual variability and trends in land surface phenology and greenness. *Global change biology* **21**, 3414-3435 (2015).

19 Keenan, T. F. & Richardson, A. D. The timing of autumn senescence is affected by the timing of spring phenology: implications for predictive models. *Global change biology* **21**, 2634-2641 (2015).

20 Buermann, W. *et al.* Widespread seasonal compensation effects of spring warming on northern plant productivity. *Nature* **562**, 110-114 (2018).

21 Shi, C. *et al.* Effects of warming on chlorophyll degradation and carbohydrate accumulation of alpine herbaceous species during plant senescence on the Tibetan Plateau. *PLoS One* **9**, e107874 (2014).

22 Fracheboud, Y. *et al.* The control of autumn senescence in European aspen. *Plant physiology* **149**, 1982-1991 (2009).

23 Schwartz, M. D. *Phenology: an integrative environmental science*. (Springer, 2003).

24 Hartmann, D. L. *et al.* in *Climate change 2013 the physical science basis: Working group I contribution to the fifth assessment report of the intergovernmental panel on climate change* 159-254 (Cambridge University Press, 2013).

25 Lian, X. *et al.* Summer soil drying exacerbated by earlier spring greening of northern vegetation. *Science advances* **6**, eaax0255 (2020).

26 Pinzon, J. E. & Tucker, C. J. A Non-Stationary 1981–2012 AVHRR NDVI3g Time Series. *Remote Sensing* **6**, 6929-6960 (2014).

27 Staff, N. C. f. A. R. in *The Climate Data Guide: NDVI: Normalized Difference Vegetation Index-3rd generation: NASA/GFSC GIMMS* (Last modified 14 Mar 2018).

28 Vermote, E. in *NOAA CDR Program, NOAA National Centers for Environmental Information* (2019).

29 Didan, K. in *MOD13C2 MODIS/Terra Vegetation Indices Monthly L3 Global 0.05Deg CMG V061. NASA EOSDIS Land Processes DAAC. https://doi.org/10.5067/MODIS/MOD13C2.061; obtained from the Land Processes Distributed Active Archive Center (LP DAAC), located at the U.S. Geological Survey (USGS) Earth Resources Observation and Science (EROS) Center (lpdaac.usgs.gov) [last access: January 26, 2022], modified and converted into netCDF file format at the Integrated Climate Data Center (ICDC), CEN, University of Hamburg, Germany.* (2021).

30 Mann, H. B. Nonparametric tests against trend. *Econometrica: Journal of the econometric society*, 245-259 (1945).

31 Kendall, M. G. Rank correlation methods. (1948).

32 Fu, Y. H. *et al.* Declining global warming effects on the phenology of spring leaf unfolding. *Nature* **526**, 104-107 (2015).

33 Julien, Y. & Sobrino, J. Global land surface phenology trends from GIMMS database. *International Journal of Remote Sensing* **30**, 3495-3513 (2009).

34 Stöckli, R. & Vidale, P. L. European plant phenology and climate as seen in a 20-year AVHRR land-surface parameter dataset. *International Journal of Remote Sensing* **25**, 3303-3330 (2004).

35 Myneni, R. B., Keeling, C., Tucker, C. J., Asrar, G. & Nemani, R. R. Increased plant growth in the northern high latitudes from 1981 to 1991. *Nature* **386**, 698-702 (1997).

36 Zhu, W. *et al.* Extension of the growing season due to delayed autumn over mid and high latitudes in North America during 1982–2006. *Global Ecology and Biogeography* **21**, 260-271 (2012).

37 Garonna, I. *et al.* Strong contribution of autumn phenology to changes in satellite-derived growing season length estimates across Europe (1982–2011). *Global Change Biology* **20**, 3457-3470 (2014).

38 Farlow, S. J. The GMDH algorithm of Ivakhnenko. *The American Statistician* **35**, 210-215 (1981).

39 Beaudoing, H. a. M. R. N. G. H. (ed Maryland Greenbelt, USA, Goddard Earth Sciences Data and Information Services Center (GES DISC)) (2016).

40 Rodell, M. *et al.* The global land data assimilation system. *Bulletin of the American Meteorological society* **85**, 381-394 (2004).

41 Rodell, M. *et al.* in *Proc. ECMWF/ELDAS Workshop on Land Surface Assimilation.* 61-68.

42 Hersbach, H. *et al.* The ERA5 global reanalysis. *Quarterly Journal of the Royal Meteorological Society* **146**, 1999-2049 (2020).

43 Martens, B. *et al.* GLEAM v3: Satellite-based land evaporation and root-zone soil moisture. *Geoscientific Model Development* **10**, 1903-1925 (2017).

44 Miralles, D. G. *et al.* Global land-surface evaporation estimated from satellite-based observations. *Hydrology and Earth System Sciences* **15**, 453-469 (2011).

45 Pastorello, G. *et al.* The FLUXNET2015 dataset and the ONEFlux processing pipeline for eddy covariance data. *Scientific Data* **7**, 225 (2020). https://doi.org:10.1038/s41597-020-0534-3

46 Forkel, M. *et al.* Enhanced seasonal CO2 exchange caused by amplified plant productivity in northern ecosystems. *Science* **351**, 696-699 (2016).

47 Brown, W. H. The relation of evaporation to the water content of the soil at the time of wilting. *The Plant World* **15**, 121-134 (1912).

48 Gao, H. *et al.* Climate controls how ecosystems size the root zone storage capacity at catchment scale. *Geophysical Research Letters* **41**, 7916-7923 (2014). https://doi.org:https://doi.org/10.1002/2014GL061668

49 Goulden, M. *et al.* Sensitivity of boreal forest carbon balance to soil thaw. *Science* **279**, 214-217 (1998).

50 Barr, A., Black, T. A. & McCaughey, H. in *Phenology of ecosystem processes* 3-34 (Springer, 2009).

51 Richardson, A. D. *et al.* Influence of spring and autumn phenological transitions on forest ecosystem productivity. *Philosophical Transactions of the Royal Society B: Biological Sciences* **365**, 3227-3246 (2010).

52 Peñuelas, J., Rutishauser, T. & Filella, I. Phenology feedbacks on climate change. *Science* **324**, 887-888 (2009).

Methods

Study area and working units: this study is conducted at the scale of the European continent (supplementary Fig. 11). We classified all pixels within Europe using the GLDAS Vegetation Class/ Mask[40] (GVC, see supplementary Fig. 11). The GVC map is available at https://ldas.gsfc.nasa.gov/gldas/vegetation-class-mask. To classify the pixels, dominant GVC land cover types were selected for further analysis. Selected land cover types include croplands, evergreen needleleaf forests, mixed forest, open shrublands, wooden tundra, grasslands, and mixed tundra. Once the work units were identified, all calculations were performed on a pixel-by-pixel basis and then the results within each work unit were averaged (wherever necessary) to obtain class-specific results.

Datasets: Data from different sources are used for this analysis. We used NDVI (Normalized Difference Vegetation Index) data from the Global Inventory Monitoring and Modelling System (GIMMS) [26,27](covering the period 1981-2015), the Advanced Very High-Resolution Radiometer (AVHRR)[28] (covering the period 1981-2020), and the Moderate Resolution Imaging Spectroradiometer (MODIS) [29] (covering the period 2001-2020) to determine the OG and OD and consequently the LGS. In addition, the NASA Global Land Data Assimilation System (GLDAS) along with the NOAH Land Surface Model[39-41] (v2.0, for 1982-2014, and v2.1, for 2000-2020), the European Centre for Medium-Range Weather Forecasts (ECMWF) ERA5- land[42] (for 1982-2020), and the Global Land Evaporation Amsterdam Model[43,44] (GLEAM v3.6a, for 1982-2020) were the three other datasets used in this analysis. We also used in situ measurement data from FLUXNET[45] (with a duration of 1995-2020) as a benchmark for the reanalysis data.

Data preprocessing: The data used in this analysis from different sources are provided at different spatial resolutions, with the coarser resolution being 0.25 degrees for GLDAS and GLEAM databases. Therefore, for consistency, we used the RegularGridInterpolator function of the interpolate sub-package of the Python package of scipy to interpolate them (wherever necessary) with a resolution of 0.25 degrees, using the same latitude and longitude vectors of the GLDAS and GLEAM databases. In the case of the NDVI data, we used the GIMMS NDVI data as a benchmark for our analysis because it is commonly used in other studies. However, it should be noted that the GIMMS NDVI data are available at biweekly temporal resolution (i.e., two data per month), the MODIS NDVI data are available at monthly resolution, and the AVHRR NDVI data are available at daily resolution. Therefore, we brought them all to monthly resolution by averaging the data that fall within each month, i.e., in the case of the GIMMS data, the two data within each month, and in the case of the AVHRR data, all daily data of each month. This was necessary because the temporal resolution of the NDVI data affects the derived OG and OD values. Additionally, we excluded the last three years of AVHRR data (2018-2020) from the analysis due to unknown quality of the data for these years.

The Princeton meteorological forcing data used for GLDAS 2.0 ends in 2014, so GLDAS 2.1 (covering 2001-present) uses other forcing data including observation-based P and solar radiation, resulting in significantly higher values nearly for all variables, as the climatology of the forcing variables differs from that of the Princeton forcing dataset. Therefore, we used the overlapping period 2001-2014 to construct location- and day of year-specific linear regressions between paired variables from v2.0 and v2.1, and then applied the developed regression to match the GLDAS 2.1 data to the climatology of GLDAS 2.0. In the case of P, day of year-specific linear regressions were not possible due to high variability and frequency of zero values, therefore we only applied site-specific linear regressions.

While the temporal resolution of the GLEAM dataset is daily, the GLDAS data are provided with a temporal resolution of 3 hours. Therefore, we averaged the 3-hourly data from GLDAS to account for the daily data. Although the ERA5-land dataset is originally provided with a spatial resolution of 0.05 degrees

and a temporal resolution of 1 hour, for consistency, we downloaded the daily and 0.25-degree resolution data using the ERA5-land Daily Statistics CDS API[1].

In cases where a variable was available from two or more of the above reanalysis products, a PCA was performed, and the first component was then used for further analyses when the target variable was in demand. This was the case for ET and SSM. In the case of ET, the first component accounted for 95 or more percent of the variation in all products, while in the case of SSM, 85 or more percent of the variation in the products used was explained by the first component.

Data validation: Before any further analysis, we validated the ET and SSM data from the datasets used (GLDAS, GLEAM and ERA5-Land) by comparing them with in situ measurement data from FLUXNET[45]. For this purpose, we extracted reanalysis data on ET and SSM for the pixels containing FLUXNET stations for the overlapping periods 2000-2020, and then performed a station-by-station comparison of the reanalysis data with the FLUXNET data. In total, 8 and 23 FLUXNET stations contain the complete data for ET from all datasets for the 2000-2009 and 2010-2020 periods, respectively, while only 4 and 18 stations have the complete data for SSM from all datasets for the 2000-2009 and 2010-2020 periods, respectively. Supplementary Fig. 12 shows the Pearson correlations between ET and SSM from FLUXNET and ET and SM from other datasets. There are strong correlations between ET from FLUXNET and ET from GLDAS, GLEAM and ERA5-land with correlation coefficients ranging from 0.59 to 0.87 for the period 2000-2009 and 0.64 to 0.91 for the period 2010-2020. In contrast to ET, the correlations between SSM from FLUXNET and SSM from GLDAS, GLEAM and ERA5-land appear to be weak (with correlation coefficients ranging from 0.24 to 0.60 for the period 2000-2009 and 0.07 to 0.83 for the period 2010-2020), partly due to the uncertainty of SSM measurements at FLUXNET stations, as seen in the large changes in SSM values or repeated constant values for some months. Overall, it seems that the reanalysis data used in this investigation can reasonably show the ongoing trend in the real world, and we can be confident that the conclusions we have drawn in this paper are valid.

LFD NDVI Method: To determine the OG and OD for individual pixels in Europe and for individual years of the entire study period (1982-2020), we needed an innovative algorithm that could operate independently for each year and pixel. This was important because classical methods, e.g., Piao et al. [53], typically calculate a critical long-term NDVI value for the entire period and then determine the timing for approaching such a critical value in all individual years. However, this was prone to bias because the NDVI data used came from three different products of GIMMS [1982-2015], AVHRR [1982-2017], and MODIS [2001-2020], especially with different temporal resolutions (biweekly, daily, and monthly), which can affect the long-term critical value and consequently the timing for OG and OD. Therefore, we developed the logistic function derivative of NDVI curve (LFD NDVI method) which can be used for each year individually. It uses the first and second derivatives of the fitted logistic function of the cumulative NDVI curve of a given year to determine the OG and OD (Extended Data Fig. 1a). As a first step, we converted all data to a monthly time scale, as mentioned earlier. Then we calculated the cumulative NDVI data over time and finally fed them into the LFD NDVI method to determine OG and OD. However, before feeding the data into the LFD NDVI method, we normalized both the NDVI and time data between 0 (min)

and 1 (max) as this was required for further calculation. Normalization of the NDVI data was done twice, once before accumulation to eliminate possible negative NDVI values, and another time after accumulation to bring them within the range of 0 to 1. In the following, the calculation with the LFD NDVI method is described in detail. When *t* and NDVI are referred to in the following, the rescaled forms are meant for the sake of simplicity.

In a first step, a logistic function was fitted to the data (Extended Data Fig. 1b):

$$y\left(t\right)=a+\frac{b}{1+\exp(-\frac{t-c}{d})}$$

1

where $y(t)$ is the cumulative NDVI on day t of the year and the model coefficients are a, b, c, and d. Using this fitted function, we obtained the smoothed curve of the cumulative NDVI data for all days of the year (t = 1:365 or 366, being scaled to 0 and 1). Third, we determined the curvature of the data, $k(t)$, for each t using the first $y'(t)$ and second $y''(t)$ derivatives of the fitted logistic function:

$$k\left(t\right)=\frac{\left|y''\left(t\right)\right|}{\left(1+y'\left(t\right)\right)^{1.5}}$$

2

Plotting $k(t)$ versus t typically showed two maxima separated by a minimum. The times at which the maxima occur allow the logistic curve to be divided into three parts with nearly linear behavior (Extended Data Fig. 1c). The first part occurs during the winter and early spring before the first curvature maximum in the data; we refer to this part as the winter dormant period. The second part occurs between the first and second curvature maxima in the data; we refer to this part as the active growth period. Finally, the third part occurs during the late summer and fall after the second curvature maximum in the data; we refer to this part as the fall dormant period.

For the second part, a first-order polynomial function was fitted by simply using the two points of maximum curvature and their respective cumulative NDVI values, plus an additional point in between. For the first and third parts, we used the sequential linear approximation method described by Dathe et al. [54] to identify the linear part of the rescaled cumulative NDVI curve before the first and after the second curvature maximum. The method consists in calculating linear regressions over a consecutive number of points before the first and after the second curvature maximum. The dependence of R^2 on the number of data points was used to determine the number of points to be included in the regression. In this analysis, an R^2 value of 0.95 was used as the critical value to determine the linear parts of winter- and fall-dormant. Next, we determined the equation of the bisector of the obtuse angle between the regression equations of the winter-dormant and active growth parts (Eq. 3) and the fall-dormant and active growth parts (Eq. 4) by computing the angle between two lines.

$$\mathrm{y}\left(\mathrm{t}\right)=a_{\mathrm{wa}}t+c_{\mathrm{wa}}$$

3

$$\mathrm{y}\left(\mathrm{t}\right)=a_{\mathrm{fa}}t+c_{\mathrm{fa}}$$

4

where a_{wa} and c_{wa} correspond to the slope and intercept of the line bisecting the lines of winter dormancy and active growth parts, and a_{fa} and c_{fa} correspond to the slope and intercept of the line bisecting the lines of fall dormancy and active growth parts. After determining the equations for the bisecting lines, the intersection between them and the fitted logistic function determines the OG and/or OD (Extended Data Fig. 1d). Mathematically, OG and OD are calculated by solving the following equations for *t*:

$$a_{\mathrm{wa}}t+c_{\mathrm{wa}}=a+\frac{b}{1+\exp(-\frac{t-c}{d})}$$

5

$$a_{\mathrm{fa}}t+c_{\mathrm{fa}}=a+\frac{b}{1+\exp(-\frac{t-c}{d})}$$

6

In this analysis, the root_scalar function of the Optimize sub-package of the Python package scipy (as an alternative to the "fzero" function in MATLAB) was used to find a null of the above expression by changing the *t* values.

Using the above-mentioned method, we determined the OG and OD from three different NDVI products of the GIMMS (for the period 1982–2015), the AVHRR (for the period 1982–2017), and the MODIS (for the period 2001–2020). Since the higher quality of GIMMS data is already well documented, we used the results obtained with GIMMS as a benchmark and compared the results from two other products to it. A scaling factor at different land use levels was used to adjust the results of the AVHRR and MODIS to GIMMS. Finally, the average values for the OG and OD from these products were used for further analysis.

Trend analysis of Mann-Kendall test: In this analysis, we examined the overall trend of OG and OD as well as LGS using the Mann-Kendall test[30,31]. To do this, we applied the Python implementation of the nonparametric Mann-Kendall trend analysis called pyMannkendal[55] employing the original and Theil-Sen methods with a significance level of 0.05. Both original and Theil-Sen methods show how the OG, OD, and/or LGS change with time, but Theil-Sen is more robust against individual outliers[56]. As suggested by Cortés et al. [56], prior to trend analysis, we dealt with temporal autocorrelation of data with AR(1)correction to prevent the occurrence of false positive rates[57]. As suggested by von Storch [57] and outlined by Cortés et al. [56], the following equation is used to calculate the temporal autocorrelations at lag -1:

$$\hat{r} = \frac{n\sum_{1}^{n-1}\left(x_t - \bar{x}\right)\left(x_{t+1} - \bar{x}\right)}{(n-1)\sum_{1}^{n}\left(x_t - \bar{x}\right)^2}$$

7

where $\hat{r}$ is autocorrelation, x_t is data at time t, $\bar{x}$ is the mean value of all data, and n is number of the data. Then, when autocorrelation is computed, the original time series (x_t) were replaced with adjusted one (y_t) using following equation:

$$y_t = x_t - \hat{r}\, x_{t-1}$$

8

Group Method of Data Handling: we applied the group method of data handling (GMDH) [38] to develop a gray box network predicting the OG and OD, and the LGS, using several meteorological variables along with soil moisture as inputs. For this purpose, we used the main meteorological variables (T, P, and VPD) plus SSM and RSM. We excluded ET and transpiration from this analysis because they are logically strongly correlated with the phenological states of vegetation and mask the importance of other variables. We also excluded climate indices (NAO: North Atlantic Oscillation, El Nino, etc.) from this analysis because the pretest showed that in this context, they play a lesser role than the other included variables. All included variables were averaged for several time periods, namely winter [January 1 to 30 days before the OG], early spring [30 days before the OG to the OG], spring [OG to the PG], summer [PG to the two weeks before the OD], and late summer [two weeks before OD to the OD]. Then, their long-term anomalies were calculated for each period and then subjected to modeling.

The following quadratic regression is used to obtain the preliminary estimates (z_{ij}) for the first layer of the GMDH network[58]:

$$z_{ij} = c_0 + c_1 x_i + c_2 x_j + c_3 x_i^2 + c_4 x_j^2 + c_5 x_i x_j$$

9

where x_i and x_j represent the pairwise selection of input variables and c_0 to c_5 represent the polynomial predictors. The following equation determines the total number (n) of possible polynomials[58]:

$$n = \frac{N \times (N-1)}{2}$$

10

where N is the number of input variables. To develop the GMDH network, we first developed all possible polynomials with pairwise selected variables (x_i and x_j). Then we had to filter out the least effective new variables using a statistical selection criterion[38]. We used the following criteria to select the best new variables to build the next layer of the network[59]:

$$e = p \times RMSE_{\text{lowest}} + (1 - p) \times RMSE_{\text{highest}}$$

11

where *p* is the selection pressure and means a number between 0 and 1 (with p = 0.75 in our analysis), with higher numbers indicating higher pressure in selecting new variables. The preliminary estimates with root mean square error (RMSE) smaller than *e* were selected for the next layer. The polynomials were then further improved by repeating steps 1 and 2 and using new selected variables (z_{ij}) from the previous step. This continues until the smallest value of the selection criterion from the current iteration shows no improvement over the smallest value from the previous iteration[58].

To develop GMDH models for predicting anomalies in LGS (the same applies for the OG and OD), we forced the models to have only one layer with two most important variables going into the model. The concept underlying this strategy is to select only two variables for each pixel for predicting the OG and OD or the LGS. To train and evaluate the developed networks, the data were randomly split into two subsets, with 70 percent of the data used to train the networks and the rest used to test as independent data.

The GMDH method provides a built-in algorithm[58,59] that retains only the essential input variables. Therefore, here we repeated 100 times the random division of the data into training and test subsets, developed the models, and calculated the Pearson correlation (R) between the target and output variables for each replication. Then, the replications with R value less than 0.7 in the evaluation subset were filtered out and the selected sets of variables for predicting the onset of the OG and OD and LGS in the remaining replications were determined. The used GMDH algorithm is coded in Python.

To visualize the results obtained from GMDH analysis, the first and second important control factors of anomalies of LGS (as well as OG and OD) are plotted against each other, and the colors show their frequency among the pixels in Europe (see supplementary Figs. 6 and 7). In this way, we were able to check which variable was the most important factor and with which other variable it usually paired to explain the anomalies in LGS (and/or OG and OD).

Principal component analysis and biplotting: To investigate the direction of the effects of the control factors on LGS as well as OG and OD, we performed PCA on the data and illustrated the result as biplots. Biplots show both the observations and the original variables in principal component space[60]. In a biplot, positively correlated variables are closely aligned, while negatively correlated variables are aligned in the opposite direction. In both cases, the stronger the correlation between variables, the larger the size of the arrows. Variables aligned at 90 degrees to each other have no correlations [61].

[1] - https://cds.climate.copernicus.eu/cdsapp#!/software/app-c3s-daily-era5-statistics?tab=overview

References

53 Piao, S., Fang, J., Zhou, L., Ciais, P. & Zhu, B. Variations in satellite-derived phenology in China's temperate vegetation. *Global change biology* **12**, 672–685 (2006).

54 Dathe, A., Eins, S., Niemeyer, J. & Gerold, G. The surface fractal dimension of the soil–pore interface as measured by image analysis. *Geoderma* **103**, 203–229 (2001). https://doi.org/10.1016/S0016-7061(01)00077-5.

55 Hussain, M. & Mahmud, I. pyMannKendall: a python package for non parametric Mann Kendall family of trend tests. *Journal of Open Source Software* **4**, 1556 (2019).

56 Cortés, J. et al. Where are global vegetation greening and browning trends significant? *Geophysical Research Letters* **48**, e2020GL091496 (2021).

57 von Storch, H. in Analysis of Climate Variability. (eds Hans von Storch & Antonio Navarra) 11–26 (Springer Berlin Heidelberg).

58 Pachepsky, Y. A. & Rawls, W. Accuracy and reliability of pedotransfer functions as affected by grouping soils. *Soil Science Society of America Journal* **63**, 1748–1757 (1999).

59 Rahmati, M. Reliable and accurate point-based prediction of cumulative infiltration using soil readily available characteristics: a comparison between GMDH, ANN, and MLR. *Journal of Hydrology* **551**, 81–91 (2017).

60 Gabriel, K. R. The biplot graphic display of matrices with application to principal component analysis. *Biometrika* **58**, 453–467 (1971).

61 Rahmati, M. et al. Development and analysis of the Soil Water Infiltration Global database. *Earth System Science Data* **10**, 1237–1263 (2018).https://doi.org:10.5194/essd-10-1237-2018.

Declarations

Acknowledgment

The authors are grateful for the guidance provided by the NASA Global Land Data Assimilation System (GLDAS) Support Team, in particular Dr. Matthew Rodell from University of Maryland, USA, and the Global Inventory Monitoring and Modeling System (GIMMS) Support Team, Dr. Stefan Kern from University of Hamburg, Germany. The authors are also grateful for the technical support provided by Horst Hardelauf, the ex-IT technician, and Dr. Andrea Schnepf at the Agrosphere Institute IBG-3, Forschungszentrum Jülich, Germany. The comments and advice of Dr. Diego Miralles (Ghent University, Belgium) are also greatly appreciated.

Contributions

M.R and H.V. conceived this study. M.R. performed all the analyses and wrote the initial manuscript. All authors contributed to interpreting results, discussion, and improvement of this paper.

Data and codes availability

During the review process, all data and codes will be made available upon request by editors and reviewers. After acceptance, we will make the data and codes available in public depositories.

Supplementary information

Supplementary Figures 1–12, supplementary Table 1, and supplementary discussion.

Figures

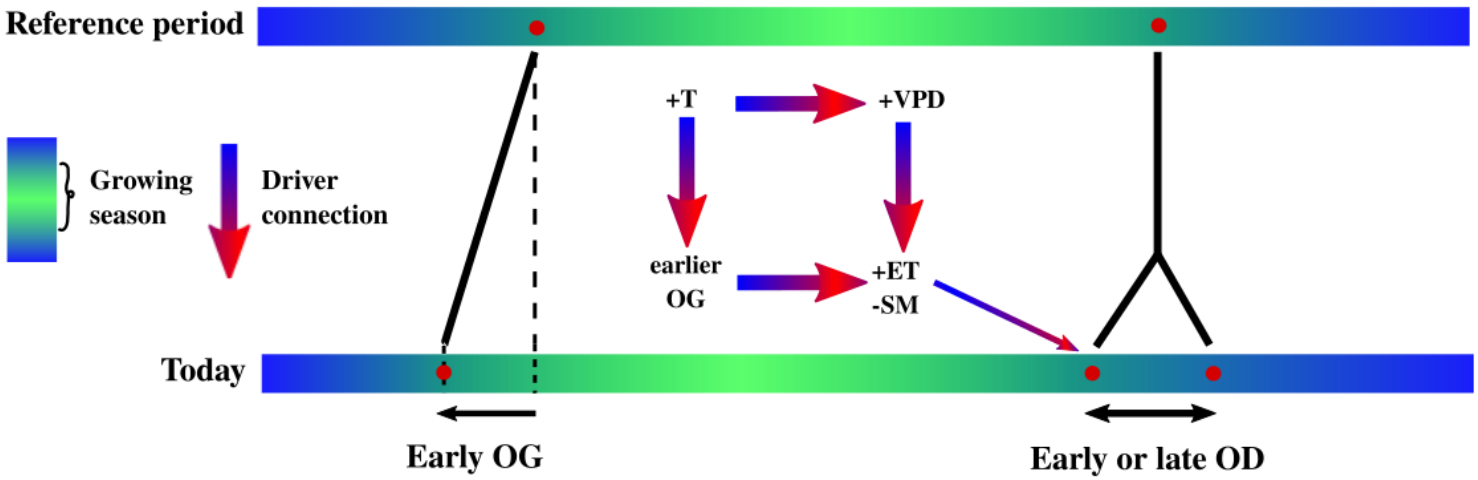

Figure 1

Schematic representation of the effects of climate change on the occurrence of onset of greening (OG) and dormancy (OD). It shows the effect of increased temperature (T) in spring on early OG and the effect of increased T in summer on increased vapor pressure deficit (VPD) and decreased soil moisture (SM) and consequently on OD. The length of the growing season (LGS) is defined as the period between OG and OD.

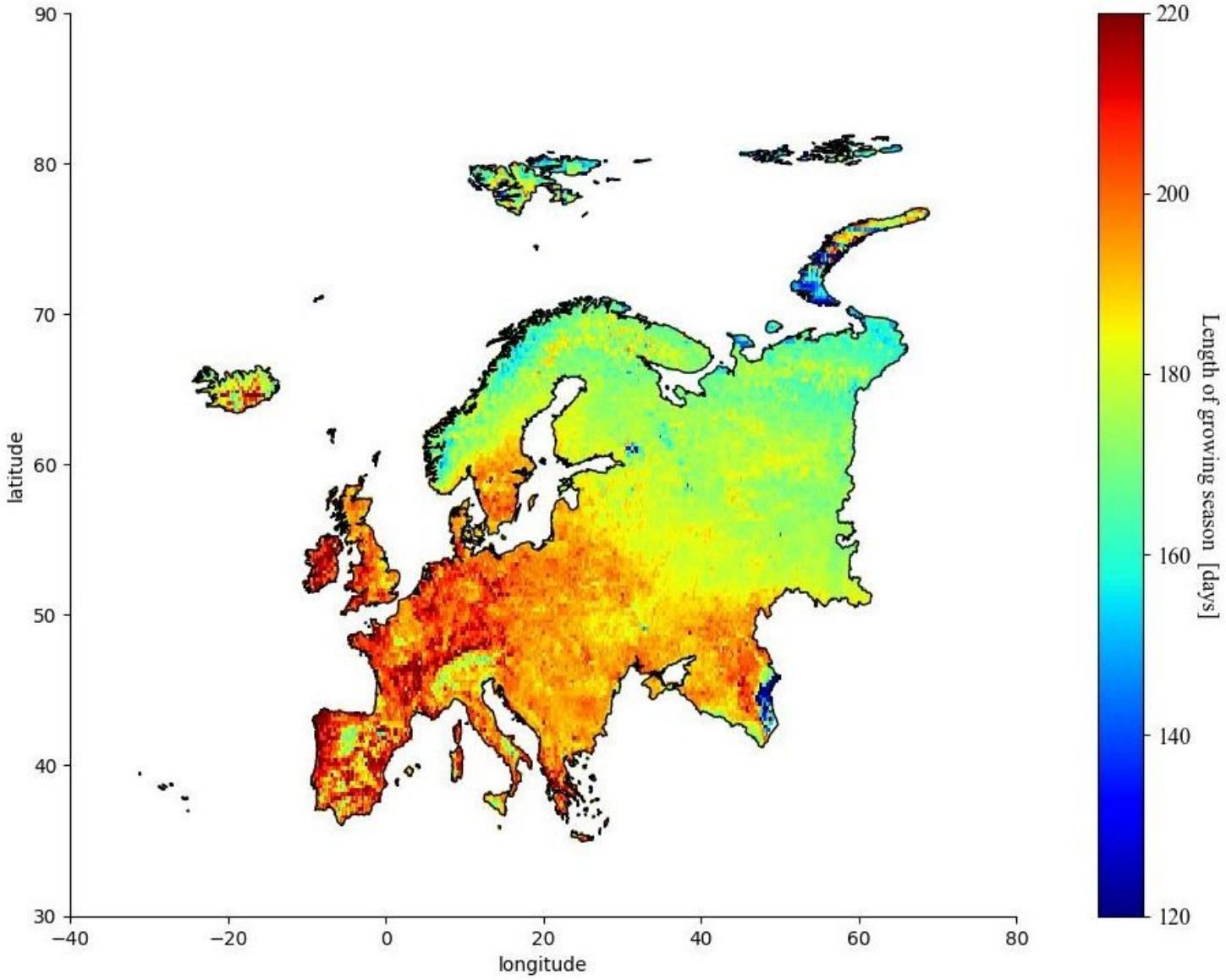

Figure 2

Spatial variation of the long-term (1982-2020) average length of growing season (LGS) in Europe.

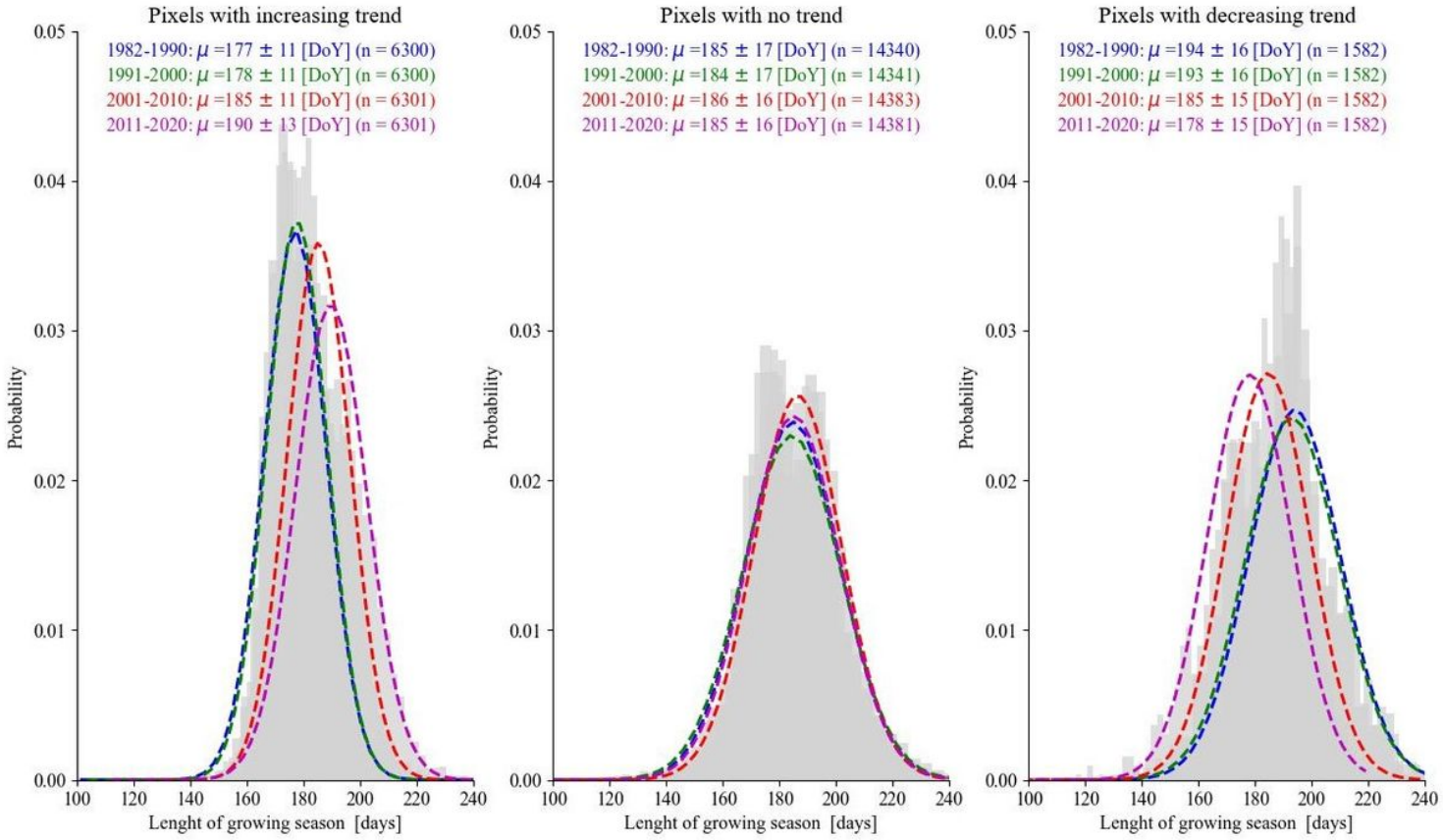

Figure 3

Histogram of the season length in different decades and different pixels with significant decreasing or increasing trend or without significant trend. The letter μ corresponds to the mean ± standard deviations.

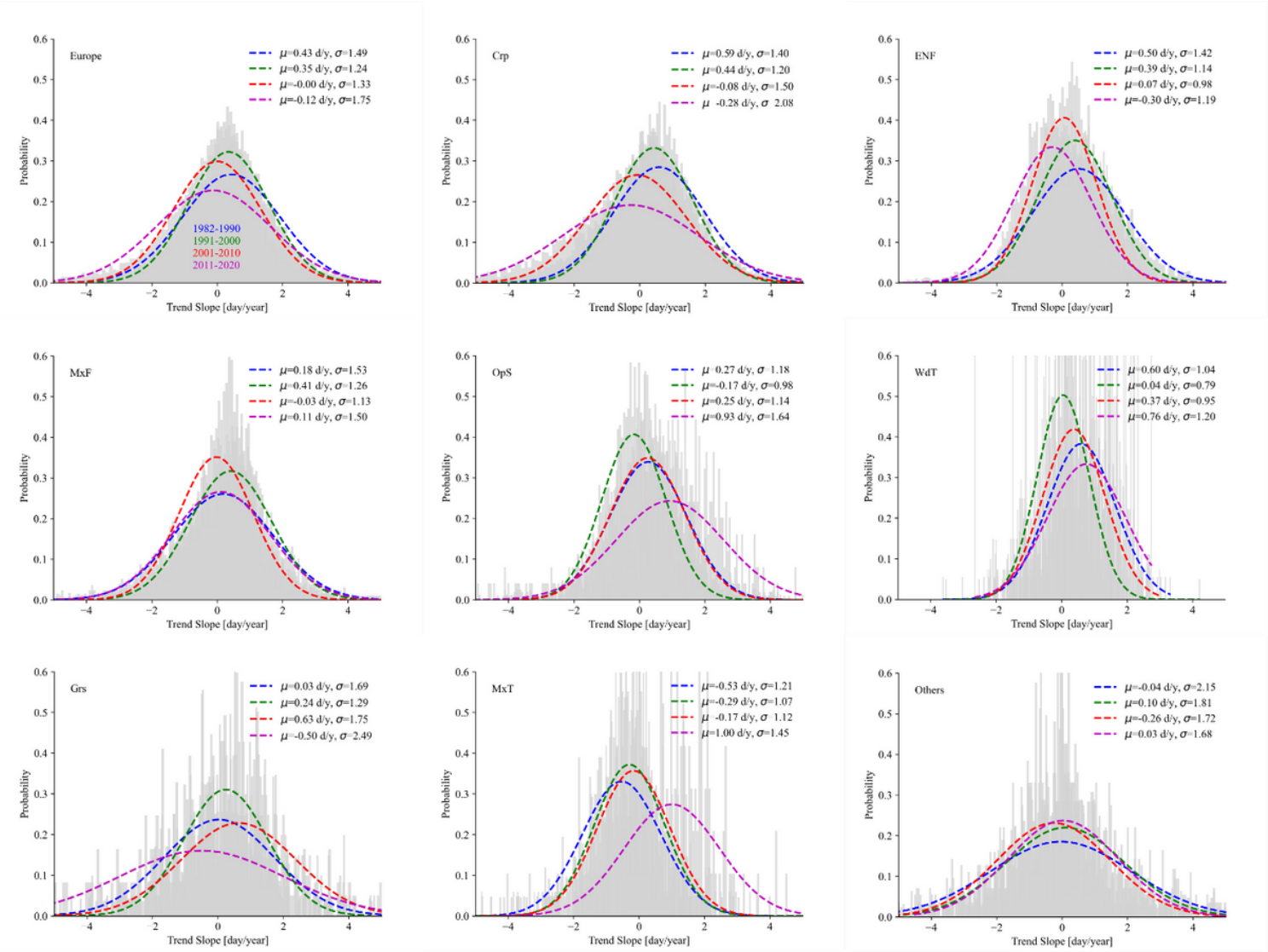

Figure 4

Histogram of changes in season length (trend parameter, from Mann-Kendall analysis) for different decades under different land cover types like croplands (Crp), evergreen needleleaf forests (ENF), mixed forest (MxF), open shrublands (OpS), wooden tundra (WdT), grasslands (Grs), and mixed tundra (MdT). The letter μ and σ correspond to the mean and standard deviations.

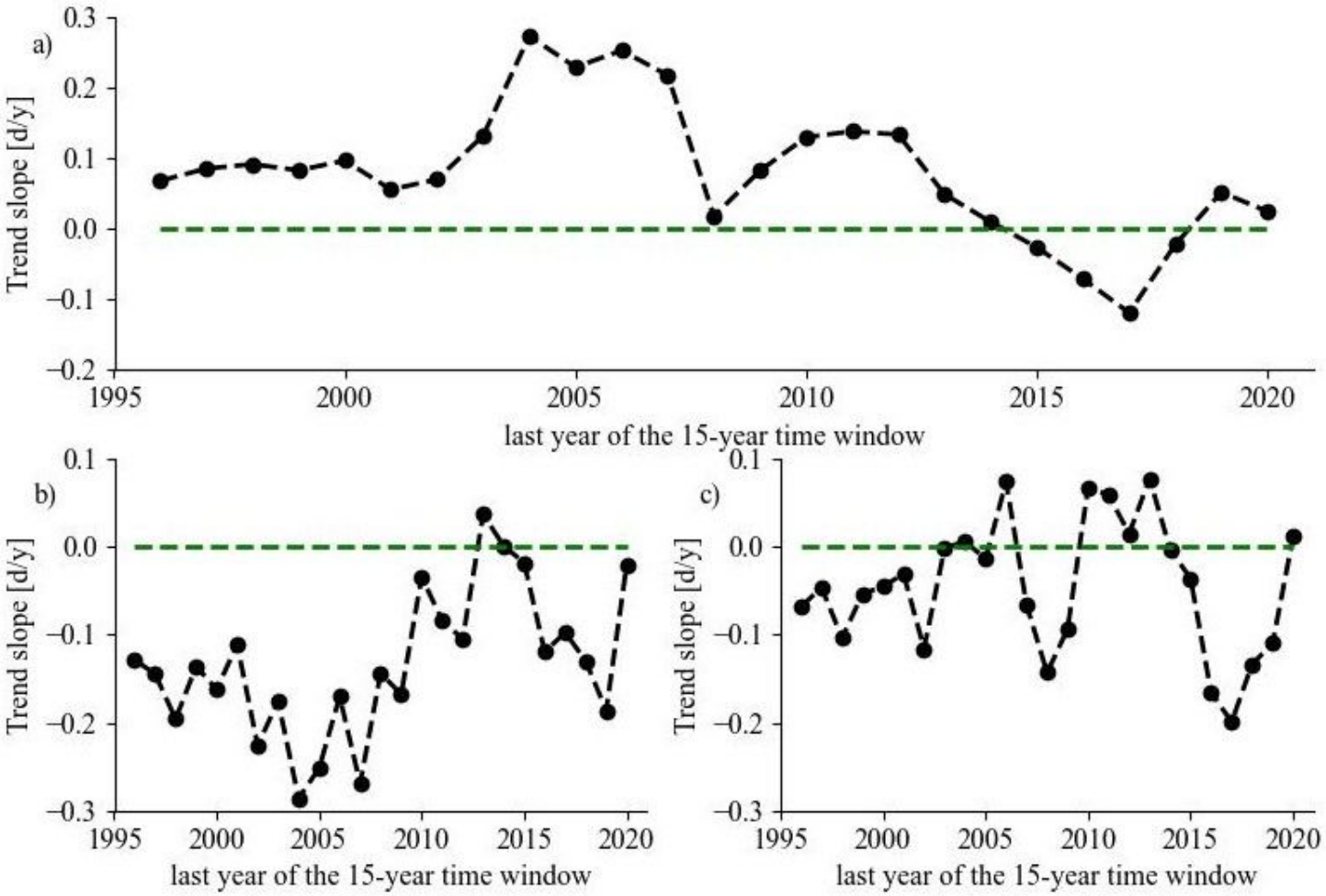

Figure 5

Variation of average trends of length of growing season (a), onset of greening (b), and onset of dormancy (c) during moving time window of 15-years from 1982-2020 in Europe.

Supplementary Files

This is a list of supplementary files associated with this preprint. Click to download.

- Supplementaryinformation.docx
- floatimage6.jpeg